SciVerse ScienceDirect

Journal of Aerosol Science

A regional, size-dependent, and causal effective medium model for Asian and Saharan mineral dust refractive index spectra

Patrick G. Stegmann[a,*], Ping Yang[a]

[a]*Department of Atmospheric Sciences, Texas A&M University, 3150 TAMU, 77840 College Station, TX, USA*

Abstract

A model is developed for the refractive index spectra of desert mineral dust. This model is applicable regionally to both Asian and Saharan dust as the largest global aerosol sources. The capability of the model further aims at representing important local features through a subdivision into northern and southern Sahara, as well as western and eastern Asia. Machine learning techniques for accelerated literature data acquisition are presented. Available refractive index spectra for individual minerals and chemical species are combined based on the Bruggeman effective medium formula. A numerical procedure for effectively solving the resulting higher-order polynomial expression is presented. The present results of the effective refractive indices are validated through the Kramers-Kronig relation; in particular, a Hilbert transform is applied to the imaginary part of the refractive index spectra.

Keywords: index of refraction; mineral dust; Sahara; Gobi; effective medium; Kramers-Kronig

* Corresponding author. Tel.: +1-979-862-4341.
E-mail address: pstegmann@tamu.edu

1. Introduction

The optical properties of terrestrial mineral dust have been a long-standing topic of investigation as evidenced by e.g. the investigations of Longtin et al. (1988) or Carlson et al. (1980) as well as Patterson et al. (1977), to name a few. During the last four decades, the interest of the respective contemporary investigations has gradually shifted from remote mineral exploration, as discussed by Egon et al. (1979) to the impact of mineral dust on the planetary radiation budget due to its relevance for the global climate and solar energy conversion in the Sahara. Similar to many scattering particles, mineral dust may reduce the radiative forcing by scattering shortwave radiation back into space, while on the other hand absorption of long wave radiation by absorbing constituents such as Hematite and soot may simultaneously have an opposite effect. The prediction of this balance between absorption and reflection giving rise to atmospheric warming and cooling respectively is still subjected to significant uncertainties. Relevant studies on the climate impact were performed by e.g. Shell et al.(2007) or Yue et al. (2009) while Schroedter-Homscheidt et al. (2013) and Polo et al. (2015) discussed the improvement of solar power production by means of adequate aerosol forecasts and specific energy conversion process adaptions.

While the Sahara is the greatest source of mineral dust aerosol (see e.g. Koven and Fung (2008) and Prospero et al. (2002) for detailed discussions), there has been an increasing interest in the Gobi desert and other Central Asian dust sources in the recent decades, primarily in connection with air quality concerns and pollution in eastern Asia. Studies on the mineral dust in this region of the globe include, for instance, Chin et al. (2003) or Ma et al. (2012). Recent efforts to measure the refractive index of Saharan dust from several locations and under controlled conditions have been performed at the AIDA chamber of the Karlsruhe Institute of Technology by Wagner et al. (2012).

Because of its significant impact of mineral dust aerosol in a variety of different areas, desert dust is a prominent component of existing databases for the optical properties of aerosols, such as OPAC by Hess et al. (1998) or the database by Levoni et al. (1997). Nevertheless, for mineral dust aerosol, the modeling of its optical properties has proven to be a formidable challenge, as the scattering dust particle is strongly heterogeneous and consists of many different mineral types and chemical species. Regional variability of the composition of mineral dust particles has been recognized in the past to further complicate the problem and studies on this topic are manifold, including the efforts by Formenti et al. (2011) and Di Biagio et al. (2014) and Ryder et al. (2013) and most notably by Dubovik et al. (2002) and Dubovik et al. (2006) with a focus on optical properties and radiative transfer.

Due to the random, heterogeneous morphologies of mineral dust particles, there is interdependence when it comes to the modeling of the shape and the refractive index of this particular type of aerosol in microphysical

light scattering computations. It has been shown by Mishchenko et al. (1997) that the nonsphericity of the dust scattering particles needs to be taken into account for single scattering calculations. Examples for the two different approaches which exist for determining the optical properties of mineral dust particles are the work by Kahnert (2004) on the one hand and the work by Liu et al. (2013) and Ishimoto et al. (2010) on the other. While Kahnert uses simple geometrical particle shapes such as spheres and spheroids and considers the heterogeneity through the refractive index, Ishimoto develops a complex random morphology model with different refractive index values specified in several disjoint particle subdivisions based on a spatial Voronoi tessellation. The effective medium approach discussed in this manuscript follows the first philosophy and allows managing the complexity involved in considering both a regional and a size-dependence of the refractive index. Based on the optical properties, the quantification of the influence of dust on radiation transport has been the subject of several studies, including Myhre and Stordal (2001) and Sokolik et al. (2001). The general consensus is that the uncertainties in the dust refractive index are the dominant source of error in the aforementioned radiation transport calculations, as discussed for instance by Myhre and Stordal (2001). Consequently, the current model aims to improve upon this situation from multiple perspectives. The spectral dependency of the refractive index on the wavelength λ of the incident light is computed as a function of the particle size, and for the first time, a rough distinction between different mineral source regions is taken into account.

This paper is organized as follows: Section 2 is the refractive index model description, further expanded upon in Sections 3 and 4, which in particular discuss data acquisition and effective medium calculation respectively. Section 5 presents the analysis of the obtained spectra in terms of the Hilbert transform or the Kramers-Kronig integral, where the first name is rather exclusive to mathematics while the second is more often encountered in physics and material science. Section 6 discusses the computation of first and second moments based on AERONET aerosol size distributions, in order to compute mean refractive index spectra independent of the particle size.

2. Refractive index model description

The theoretical basis for the model developed in this study can be found in the work of Otto et al. (2009). To compute the solar radiative effects of a Saharan dust plume, these authors developed a refractive index model based on chemical composition data for northern Saharan dust as a function of particle geometrical size published by Kandler et al. (2009). The distinctive feature of the current model is a quite useful computational tool to take the size dependence and the regional variation as parameters influencing the refractive index into

79 account by applying the same procedure as Otto et al. (2009) to different geographical regions where
80 sufficient composition data of mineral dust is available.
81 Generally, the model requires the chemical composition of a mineral dust particle as an input. The
82 composition needs to be provided in terms of the volume fraction of the particle's constituent minerals over
83 the geometric diameter. Based on these volume abundance ratios, the refractive index spectra of the individual
84 minerals can be combined in various ways. As argued by Kandler et al. (2009), the lack of cohesive refractive
85 index spectra from different authors for many mineral components, as well as the overall sheer number of
86 different mineral types further force the introduction of a simplified constituent model, where the individual
87 mineral types are merged to overarching mineral classes such as e.g. a Silicate class combining Illite,
88 Kaolinite and Chlorite. The different mineral classes into which the individual mineral types are classified are
89 listed in Table 1 and are largely identical with the classification scheme proposed by Kandler et al. (2009).
90 Additional substances included in the internal mixing, such as water, are considered as separate categories.

91 Table 1. Mineral Classes of the Model

Class	Mineral Component
Carbonates	Limestone
	Calcite
Iron Oxides	Hematite ord. & ext.
	Magnetite
	Wuestite
	Goethite
Quartz	Amorphous Quartz
	Crystalline Quartz ord. & ext.
Silicates	Illite
	Kaolinite
	Chlorite
	Serpentine
Soot	Propane soot
	Diesel soot (heated and unheated)
Sulphates	Pyrolytic Graphite
	Amorphous Carbon
	Gypsum
	Ammonium Sulphate
	Sulphuric Acid

92

As an example, the relative volume abundance for the mineral groups in the northern Sahara as measured by Kandler et al. (2009) is shown in Fig. 1. It may be observed that the volume fraction of all components changes drastically versus particle diameter, except for the iron oxides, whith low concentration remains without significant variations in magnitude.

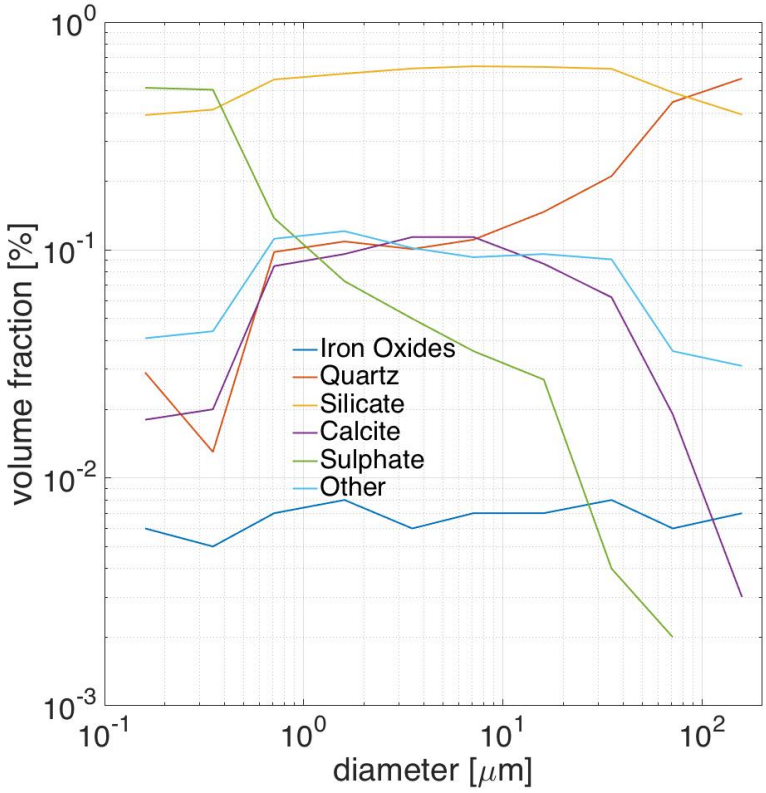

Fig. 1. Relative volume abundance over the geometrical diameter of a desert mineral dust particle from Kandler et al. (2009).

The next necessary input for the model are the refractive index spectra of the individual mineral types. These spectra often are available only piecewise for certain bandwidths and/or refractive index measurements from different sources in the literature for the same mineral under identical conditions differ by a non-negligible amount. Consequently, a sufficiently large collection of spectra from different experimental investigations needs to be collected and combined to a global patchwork spectrum. A collection of different measurements from different authors is shown in Figs. 2 and 3 and the already mentioned issues regarding the refractive index data available in the literature may be observed directly. The figures show the real and imaginary refractive index spectra from the Silicate class, respectively. The sources for both the regional size-

dependent composition data, as well as the measured refractive index spectra for the individual mineral components are given in the next Section.

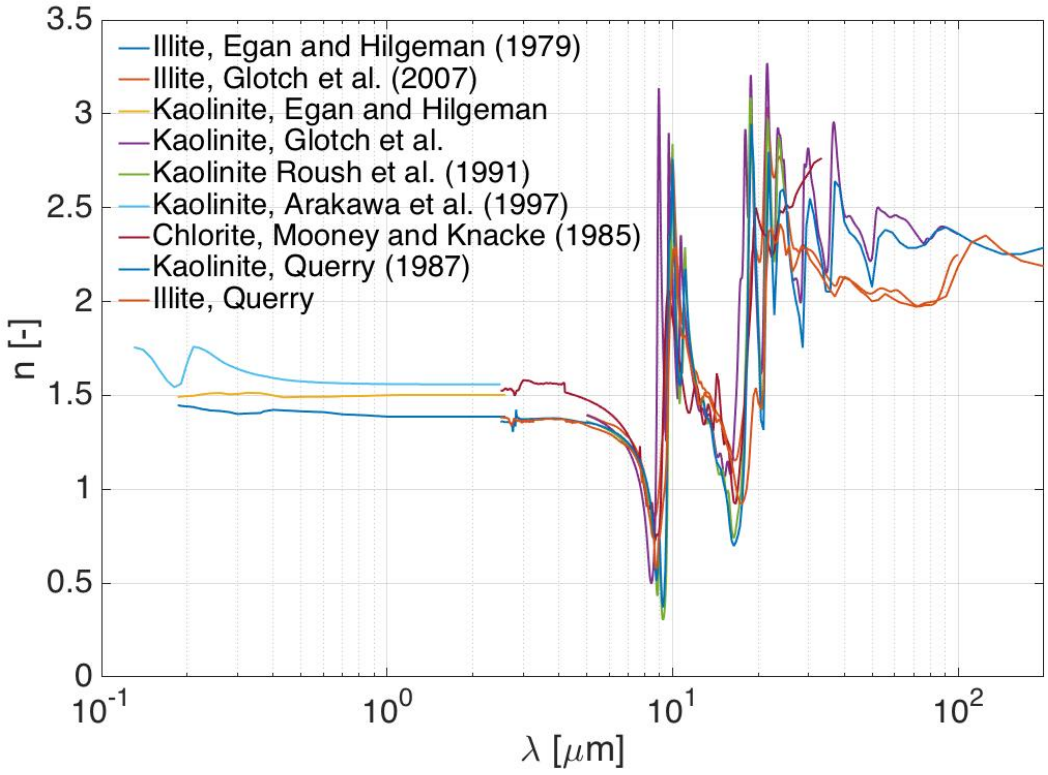

Fig. 2. Real part n(λ) of the refractive index spectrum of the Silicate group over the wavelength. Note the considerable difference between results from different studies.

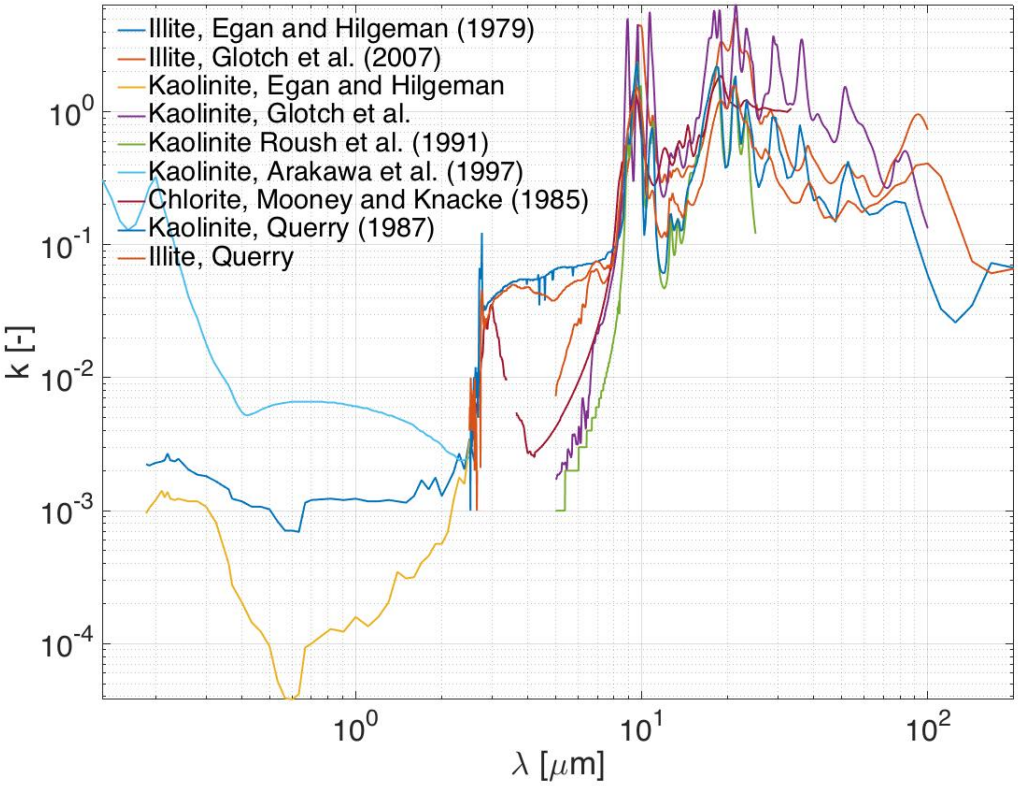

Fig. 3. Imaginary part k(λ) of the refractive index spectrum of the Silicate group over the wavelength. Considerable differences are again noticed in comparing the results obtained by different studies.

As there is no robust criterion to determine the quality and plausibility of a specific measurement versus other counterparts, the data points have been interpreted as random noise and combined spectra have been filtered using a local regression method. In practice, this amounts to low-pass filtering the literature values and the real and imaginary parts of an example of a filtered spectrum obtained from the data in Figs. 2 and 3 are shown in Figs. 4 and 5, respectively.

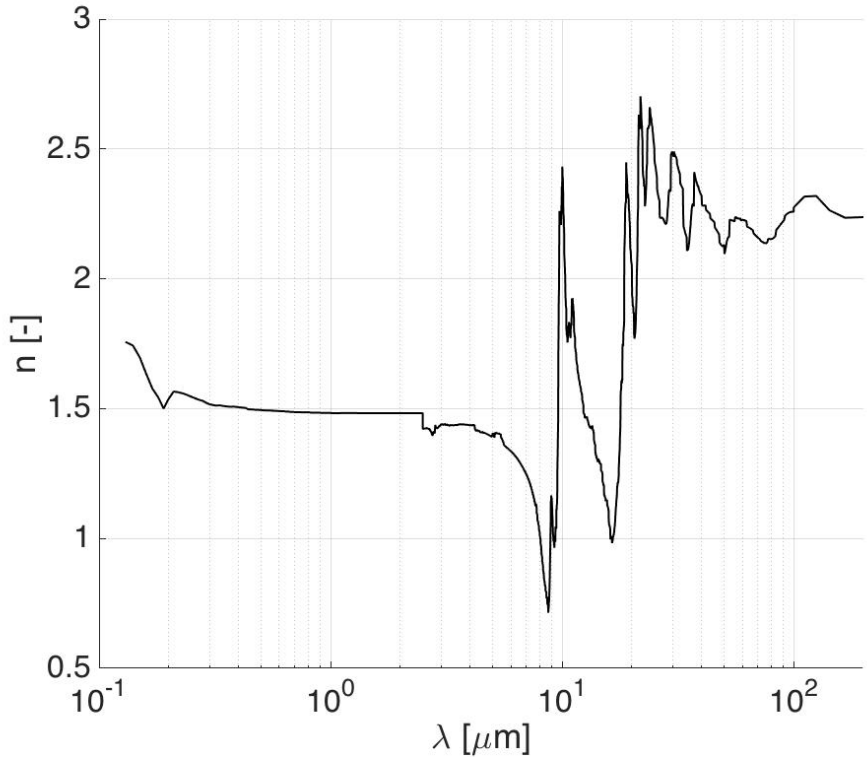

120

121 Fig. 4. Filtered real part n(λ) of the refractive index spectrum of the Silicate group over the wavelength.

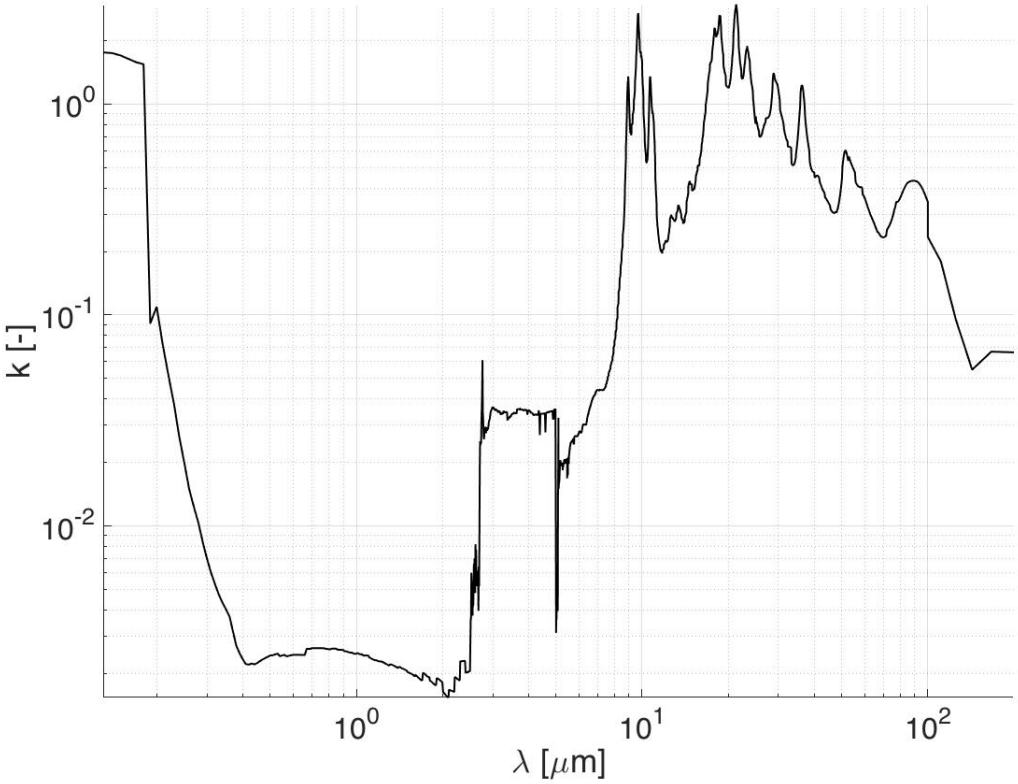

Fig. 5. Filtered imaginary part k(λ) of the refractive index spectrum of the Silicate group over the wavelength.

The obtained filtered spectra of the individual mineral groups may then be combined into *effective* spectra for a chosen mineral dust particle composition, such as the one shown in Fig. 1. Thus the dependence of the refractive index on particle size and origin is realized. Details on how to compute such an effective spectrum is given in Section 4. As the spectra computed in such an ad-hoc manner may not be consistent and certainly contain artifacts of the filtering operation, it is necessary to ensure that the spectra are analytic. This is done via a Hilbert transform or equivalently termed Kramers-Kronig analysis, as detailed in Section 5. Resulting effective spectra together with their Hilbert transformed counterparts are shown in Sections 4 and 5.

3. Data acquisition

3.1. Data sources

The current section presents the sources and methods applied in collecting the data necessary to develop the model. As all data, both concerning the mineral dust particle composition, as well as the individual refractive index spectra have been measured and not derived from first principles in any way, it should be emphasized that the model at hand is purely empirical. Based on the overview of the combination process for the mineral refractive index given in Section 2, both data for the mineral dust particle composition as well as the refractive index spectra of the individual component mineral groups are needed. The composition data are size dependent and the list of available geographical regions is given in Table 2. Again, a graphical visualization of such a data set is given in Fig. 1. Care has been taken to choose measurements performed on the ground. The measurement data from Kandler et al. (2009) are available on the ground and at altitude in the boundary layer, but the difference of the two data sets is not as significant as between different regions. While the distinction in these four regions is a coarse one due to the complexity involved in introducing a new region to the model, as well as the scarcity of chemical composition data, it is by no means arbitrary, as studies by Di Biagio et al. (2014) document the impact of the variability of African mineral dust on radiative transfer and the work of Mori et al. (2003) shows the change in chemical composition of Asian dust while being transported from the source regions in the west to the Pacific ocean in the east. Furthermore, it is understood that the data listed in Table 2 stem from point measurements and may or may not be representative for the mineral composition of the dust aerosol in the entire geographical region.

Table 2. Literature sources for mineral dust composition based on region

Geographical Region	Literature Source
Northern Sahara/Morocco	Kandler et al. (2009)
	Wagner et al. (2012)
Southern Sahara	Di Biagio et al. (2014) Klaver et al. (2011)
	Wagner et al. (2012)
Western Asia/Gobi	Mori et al. (2003)
Eastern Asia/South Korea	Geng et al. (2009)
	Mori et al. (2003)

152 The refractive index spectra for the individual mineral groups have been computed along the lines of the
153 procedure outlined in Section 2. Table 3 lists the available mineral dust aerosol component spectra together
154 with their respective literature sources and valid wavelength ranges.

155 Table 3. Literature sources for refractive index spectra of constituent mineral groups

Mineral Type or Chemical Species	Literature Source	Wavelength Range [μm]
Carbonates	Querry et al. (1978)	2.5-200
	Long et al. (1993)	2.5-333.33
	Ivlev and Popova (1972)	0.2-6
	Tropf (1998)	2-20
	Jarzembski et al. (2003)	2-20
	Jurewicz et al. (2003)	0.6-62
Iron Oxides	Shettle and Fenn (1979)	0.2-300
	Henning et al. (1995)	0.5-200
	Bedidi and Cervelle (1993)	0.45-0.75
	Gillespie and Lindberg (1992)	0.25-0.7
	Querry (1985)	0.21-55.556
	Querry et al. (1978)	2-32.8
	Popova et al. (1972)	8.3-50
	Marra et al. (2005)	5-100
	Onari et al. (1977)	5.16-50
	Steyer et al. (1974)	4-250
	Glotch et al. (2007)	
Quartz	Popova et al. (1972)	8.3-50
	Steyer et al. (1974)	7.14-25
	Peterson and Weinman (1969)	0.736-36
	Ivlev and Popova (1972)	0.2-6
	Philipp (1985)	2-25
	Shettle and Fenn (1979)	0.2-300
	Zukic et al. (1990)	125-230
	Henning et al. (1995)	6.7-408
	Malitson (1965)	0.2-4
Silicates	Egan and Hilgeman (1979)	0.185-2.6
	Roush et al. (1991)	5-25
	Querry (1987)	2.5-200
	Arakawa et al. (1997)	0.13-2.5
	Glotch et al. (2007)	5-100
	Mooney and Knacke (1985)	2.5-50

Soot	Toon et al. (1977)	0.3-40
	Shettle and Fenn (1979)	2-20
	Batten (1984)	0.5-0.75
	Blokh (1988)	1-6
	Chang and Charalampopoulos (1990)	0.4-55
	Stagg (1993)	0.4-0.7
Sulphates	Querry (1987)	2.5-200
	Palmer and Williams (1975)	2.5-25
	Volz (1973)	2.5-40
	Toon et al. (1976)	0.3-40
	Long et al. (1993)	2.5-333.33
	Ivlev and Popova (1972)	0.2-6

3.2. Artificial neural networks for automatic literature data acquisition

Especially in the current case of large datasets which need to be obtained from strongly diverse and unformatted data sources such as low-quality scanned PDF or image files and data tables found in tomes, maximizing the efficiency while minimizing the error in acquiring the desired data is of outmost importance. As a discipline of computer science, machine learning has established itself in the recent years and its techniques have proven to be essential for the construction of the present model. For a general overview on machine learning methods applied to data acquisition, the reader is referred to Hasti et al. (2009) or Harrington (2012). The specific problem to be solved in the context of this work is reading floating point numbers representing the refractive index from an image produced from a scanned PDF or the page of a book and distinguishing these numbers from the surrounding text. This problem is known as Optical Character Recognition (OCR) in Information Science. In practice, several options with varying degrees of efficiency and implementation effort are available to solve this problem. The image may be read in using the OpenCV library described by Bradski (2000) and the subsequent inference of the floating point numbers from the image may be achieved using the k-means algorithm (see Harrington (2012) for details) implemented in the OpenCV library itself, or using a less error-prone convolutional neural network (CNN) instead, available for instance in Google's TensorFlow library described in the whitepaper by Abadi et al. (2015). While k-means has a higher misidentification quota compared to the CNN, both approaches share the disadvantage of necessary prior training of the classifier before the actual application. The final approach chosen was the application of the Tesseract OCR Engine library supported by Google and described by Smith (2007). The library performs image processing and character recognition internally and is one of the most accurate open-source OCR engines to date. A sample result of OCR using Tesseract is shown in Fig. 6. A vertical column of floating-

178 point numbers is shown in a PNG image file to the left. To the right are identical numbers in a plain text
179 output file produced by the OCR code when applied to the PNG image file.

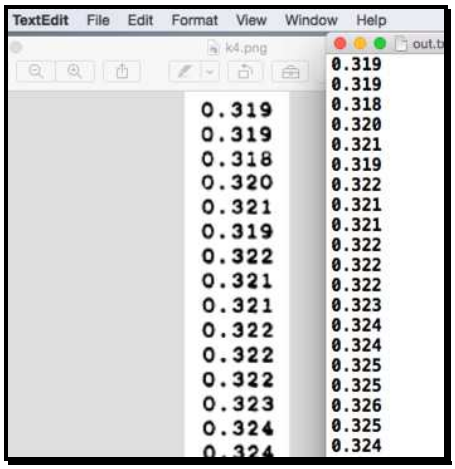

180

181 Fig. 6. Comparison of refractive index spectrum floating point numbers displayed in an image file on the left and inferred from the same
182 image in plain text form on the right, using an OCR engine.

183 **4. Effective medium approximation calculations**

184 The current section compares different available effective medium approximations. After the rationale for
185 choosing the Bruggeman formula has been elucidated, techniques for solving this higher order polynomial are
186 presented in the second part of this section.

187 *4.1. Effective medium approximations*

188 Previous works concerned with the calculation of the refractive index of mineral dust aerosols such as
189 Levoni et al. (1997), or Klaver et al. (2011), or Otto et al. (2009), and Petzold et al. (2009) have
190 predominantly relied upon the application of the volume-weighted average of the components to compute an
191 effective index:

192 $$m_{eff} = \sum_j f_j \cdot m_j \qquad (1)$$

193 where $m_{eff} = (n + i \cdot k) \in C$ is the effective complex refractive index of the mineral mixture, f_j the volume
194 fraction of component mineral *j,* and m_j the refractive index of the relevant component. The undeniable
195 advantage of this approach is its simplicity, but several other methods for the calculation of effective indices

196 with a more rigorous physical footing are known from the field of the mathematical description of
197 heterogeneous materials. The simplest of these models are called effective medium approximations (EMAs),
198 following Sahimi (2003). A formula for the effective electric permittivity ε of a matrix medium ε_m with small
199 spherical inclusions ε_i was developed by Maxwell Garnett (1904) and offers comparable simplicity to Eq.
200 (1):

201 $$\left(\frac{\varepsilon_{eff}-\varepsilon_m}{\varepsilon_{eff}+2\varepsilon_m}\right)=f_i\left(\frac{\varepsilon_i-\varepsilon_m}{\varepsilon_i+2\varepsilon_m}\right) \tag{2}$$

202 Nevertheless, the formula is only applicable to exactly two material components, one being the inclusion with
203 a volume fraction much smaller than the host medium. A well-known alternative is the formula of Bruggeman
204 (1935), which does not suffer these two restrictions but is still restricted to quasi-homogeneous materials, as
205 pointed out by Bruggeman himself. The formula most often used is in fact the formula derived by Bruggeman
206 in the case of a mixture of spherules:

207 $$\sum_{j=1}^{N} f_j \frac{\varepsilon_j-\varepsilon_{eff}}{\varepsilon_j+2\varepsilon_{eff}}=0 \tag{3}$$

208 where N is the total number of components of the heterogeneous material. In addition to Eq. (3), Bruggeman
209 has also derived different expressions for average permittivity for mixtures of prisms, cylinders and fibers.
210 Equation (3) can be reformulated to emphasise its polynomial character:

211 $$\sum_{j=1}^{N} f_j \frac{\varepsilon_j-\varepsilon_{eff}}{\varepsilon_j+2\varepsilon_{eff}}=\sum_{j=1}^{N} f_j\cdot\left(\varepsilon_j-\varepsilon_{eff}\right)\cdot\prod_{\substack{h\neq j\\ h=1}}^{N}\left(\varepsilon_h+2\varepsilon_{eff}\right)=0 \tag{4}$$

212 Equation (4) reveals a number of problems when trying to find a solution ε_{eff} for the seemingly harmless
213 polynomial in Eq. (3). By inspection of Table 3 in the preceding section one finds that one needs to solve a
214 polynomial of degree N=6 in the current case. Following Abel's impossibility theorem from Abel (1881),
215 there exists no solution for the problem at hand in terms of an algebraic expression, as N > 4. Furthermore,
216 Eq. (4) of degree N has exactly N solutions due to the fundamental theorem of algebra and one would have to
217 devise a way to find the actual physically relevant solution of Eq. (4) and distinguish it from the others. How
218 these difficulties are dealt within the context of the current project is explained in the next subsection.

4.2. Solving the Bruggeman equation

An immediate and simple solution approach is an iterative one in terms of a sequence. Equation (3) can be rearranged into the following iteration scheme:

$$\varepsilon_{eff}^{n+1} = \frac{\sum_{j=1}^{N} \frac{f_j \varepsilon_j}{\varepsilon_j + 2\varepsilon_{eff}^{n}}}{\sum_{j=1}^{N} \frac{f_j}{\varepsilon_j + 2\varepsilon_{eff}^{n}}} \tag{5}$$

with Eq. (1) as the volume weighted average being the initial guess to Eq. (5). However, no statement can be made about the monotonicity and consequently the convergence properties of the sequence, especially in the case that Eq. (1) as the initial guess differs considerably from the actual solution.

An alternative solution is to observe the change of the dielectric permittivity as the volume fraction of inclusions is gradually increased from zero. To this end, the requirement that the volume fractions of all mixture components add up to one is initially dropped. A real parameter s is introduced, such that:

$$\begin{aligned} f_1(s) &= f_1 \quad for\ j = 1 \\ f_j(s) &= s \cdot f_j \quad for\ j = 2...N \end{aligned} \tag{6}$$

To obtain differential equation governing the change of the dielectric permittivity ε_{eff} with respect to the newly introduced parameter s, Eq. (6) is inserted into Eq. (3), which is then differentiated with respect to s and the resulting ordinary differential equation is:

$$\frac{d\varepsilon_{eff}(s)}{ds} = \frac{1}{3} \cdot \frac{\sum_{j=2}^{N} f_j \frac{\varepsilon_j - \varepsilon_{eff}(s)}{\varepsilon_j + 2\varepsilon_{eff}(s)}}{\sum_{j=1}^{N} f_j(s) \frac{\varepsilon_j}{\left[\varepsilon_j + 2\varepsilon_{eff}(s)\right]^2}} \tag{7}$$

Equation (7) is then integrated over the parameter range $s = 0$ (homogeneous material) to $s = 1$ (full mixture). As no symmetries under one-parameter group transformations for the ODE are immediately obvious, including translation and dilation, no integrating factor could be found and Eq. (7) had to be integrated numerically. This was done using a standard Runge-Kutta 45 implementation from the boost odeint C++

library by Ahnert and Mulansky (2011). As the right hand side of the first order ODE is continuous and differentiable with respect to *s*, it follows from the Picard-Lindelöf theorem by Lindelöf (1894) that the solution to the initial value problem posed by Eq. (7) exists and, in contrast to the solutions of the polynomial in Eq. (4), also is unique. The refractive index is then obtained from the permittivity by taking the square root:

$$m_{eff} = \sqrt{\varepsilon_{eff}} \tag{8}$$

Conceptually, the approach involving Eq. (7) can be seen as an application of the so-called invariant imbedding technique to the computation of the effective refractive index (see Bellman and Wing (1975) for a mathematical review), which is used to great effect in single scattering calculations by Bi et al. (2013) and multiple scattering by e.g. Natsuyama et al. (1998).

4.3. Results

The current subsection shows computed refractive index spectra calculated using the methods explained in the previous subsection. A comparison between the Bruggeman EMA results and the simple volumetric average for a 0.5-μm dust particle from the northern Sahara is shown in Figs. 7a and 8a. While the solutions based on the two methods for the real part and the shortwave segment of the imaginary part are in reasonable agreement, the spectra in the long wave region of the imaginary part diverge. The Bruggeman EMA shows a decreasing trend of the imaginary part, while the Volumetric Averaging shows an increasing trend. As the particle composition at a size of 0.5 μm is dominated by the silicate and sulphate group as can be seen from Fig. 1, the decreasing trend of the EMA is the correct behavior that one might expect from the spectra of the component mineral groups. Thus in light scattering and radiative transfer calculation, the Volumetric Averaging would lead to an overestimation of the absorption in the long wave region relative to the Bruggeman EMA. The decadic logarithm of the absolute difference between the spectra obtained using the two different methods shown in Figs. 7b and 8b for the real and imaginary part respectively also reveals that the two methods also tend to disagree in particular at the resonances of the refractive index spectra.

The real part of a Bruggeman EMA spectrum for a dust particle from the northern Sahara is shown in Fig. 9. The different superimposed spectra are for a range of particle sizes, showing clearly the strong variation of the refractive index with particle size and thus mineral composition. While no appreciable difference can be observed below a wavelength of 6 micrometers, irregular changes are observed above this threshold. There is no general tendency of the refractive index either being increased or decreased with size, but the resonances of the spectrum generally become more pronounced with increasing particle diameter.

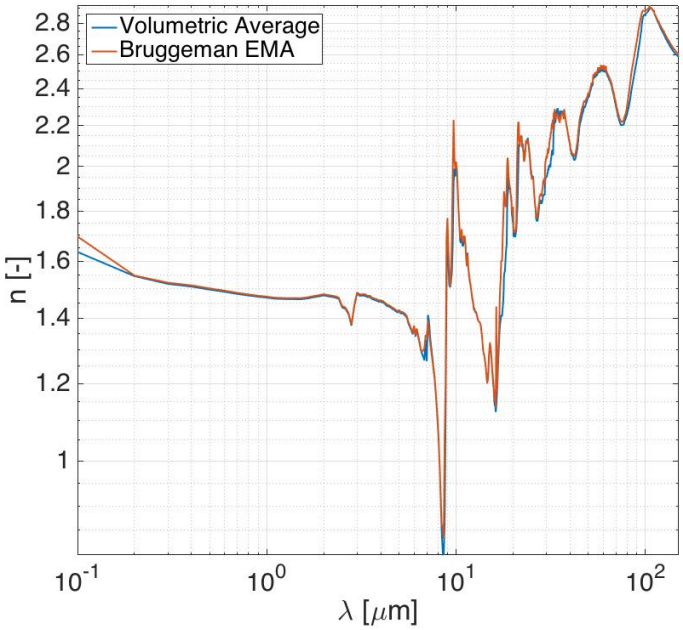

Fig. 7a. Direct comparison of real index of refraction from Volumetric Average and EMA.

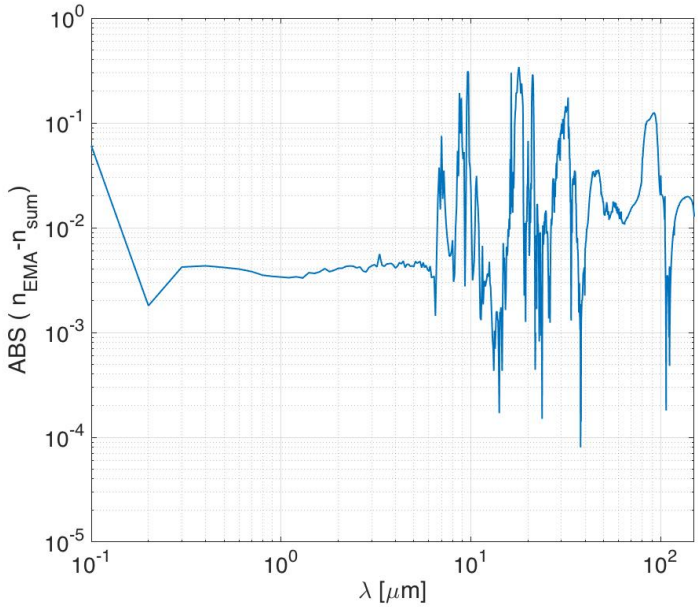

Fig. 7b. Decadic logarithm of the absolute difference of the real index of refraction from EMA and Volumetric Average.

Fig. 7. Comparison of refractive index spectra (real part) obtained using the Bruggeman EMA (red curve in Fig. 7a) through solving Eq. (7) and simple volumetric addition (red curve in Fig. 7a) through solving Eq. (1) for a particle size of 0.5 μm in the Northern Sahara.

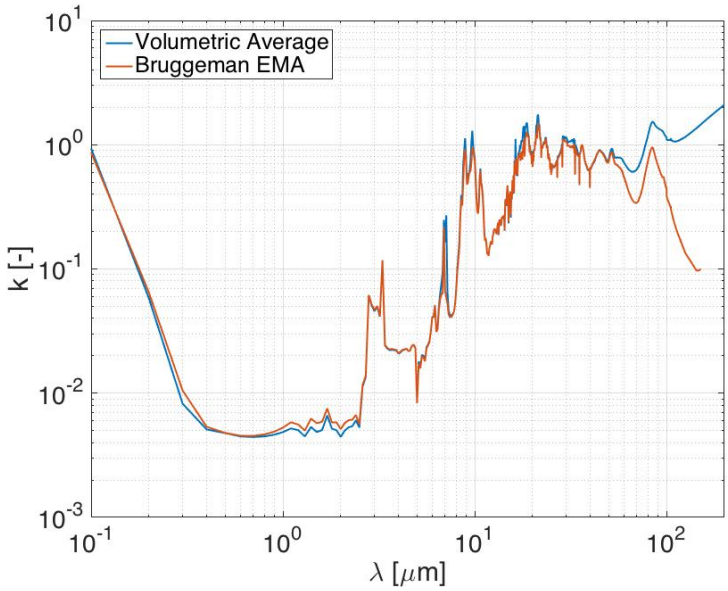

Fig. 8a. Direct comparison of imaginary index of refraction from Volumetric Average and EMA.

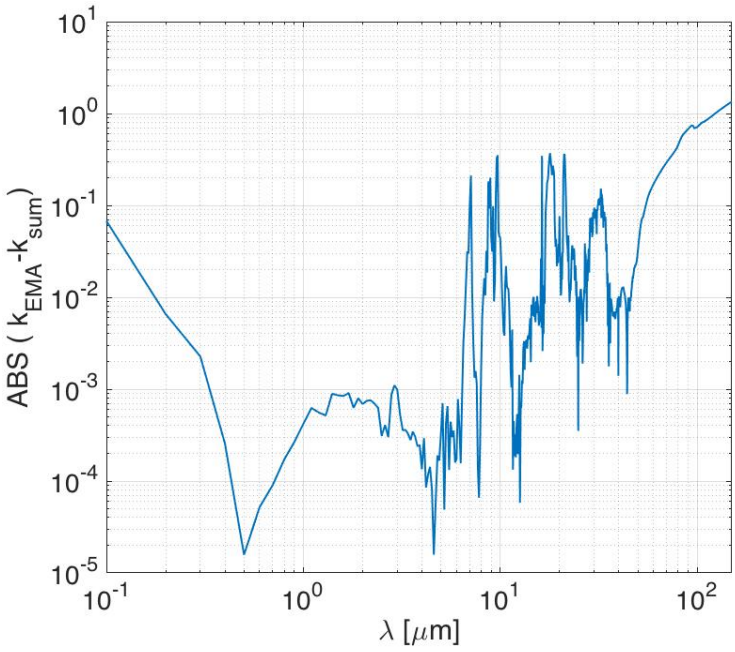

Fig. 8b. Decadic logarithm of the absolute difference of the imaginary index of refraction from EMA and Volumetric Average.

Fig. 8. Comparison of refractive index spectra (imaginary part) obtained using the Bruggeman EMA (red curve in Fig. 7a) through solving Eq. (7) and simple volumetric addition (red curve in Fig. 7a) through solving Eq. (1) for a particle size of 0.5 μm in the Northern Sahara.

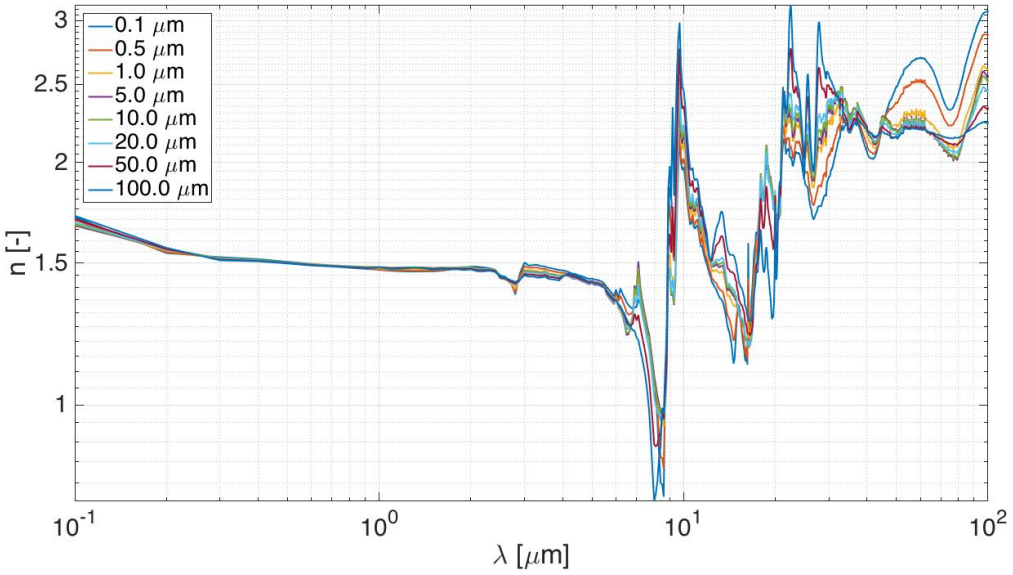

Fig. 9. Comparison of the real part of the refractive index spectrum of a northern Sahara dust aerosol particle for various particle sizes and thus mineral compositions computed using the Bruggeman EMA.

5. Hilbert transform analysis

As all obtained refractive index spectra must be regarded as a disjoint patchwork with numerical artifacts from the filtering procedure, measures need to be taken in order to ensure that the results of the effective medium and filtering operations remain physically meaningful and causal. This is done by enforcing the Kramers-Kronig (KK) relationship on the imaginary part of an effective refractive index spectrum. The imaginary part of a given refractive index spectrum for a specific particle size and geographic location is transformed into the real part via a Hilbert transform, as the imaginary part is generally considered to be measurable with a higher degree of precision than the real part.

5.1. Warren's method for Kramers-Kronig transforms

The specific Kramers-Kronig transform applied is the first integral relation proposed by Warren (1984) and later used by Iwabuchi and Yang (2011). In both cases the integral has been applied to compute the real part of the refractive index of water ice from its imaginary part. The transform itself is given by the following expression:

$$n(\nu) = 1 + \frac{2}{\pi} P \int_0^\infty \frac{\kappa^2 \cdot k(\kappa) - \nu \cdot \kappa \cdot k(\nu)}{\kappa^2 - \nu^2} d\ln\kappa \tag{9}$$

where $\nu = 1/\lambda$ is the wavenumber and P denotes the Cauchy principal value. As pointed out by Warren (1984), Eq. (9) is equivalent to the conventional formulation of the Kramers-Kronig relation, but with a singularity of type 0/0. The integral of Eq. (9) in practice is carried out using a simple trapezoidal rule. Again, the sampling of the quadrature points is done equally spaced in $\ln\kappa$. The integral over the interval containing the mentioned singularity at $\nu = \kappa$ is carried out analytically following the procedure outlined by Warren (1984). We confirm the finding of Warren (1984) that the contribution of the singularity to the quadrature is in practice negligible for a sufficiently fine grid; nevertheless the computational burden of evaluating the integral in the singularity interval is minuscule. The slow but steady convergence of the trapezoidal quadrature is shown in Fig. 10.

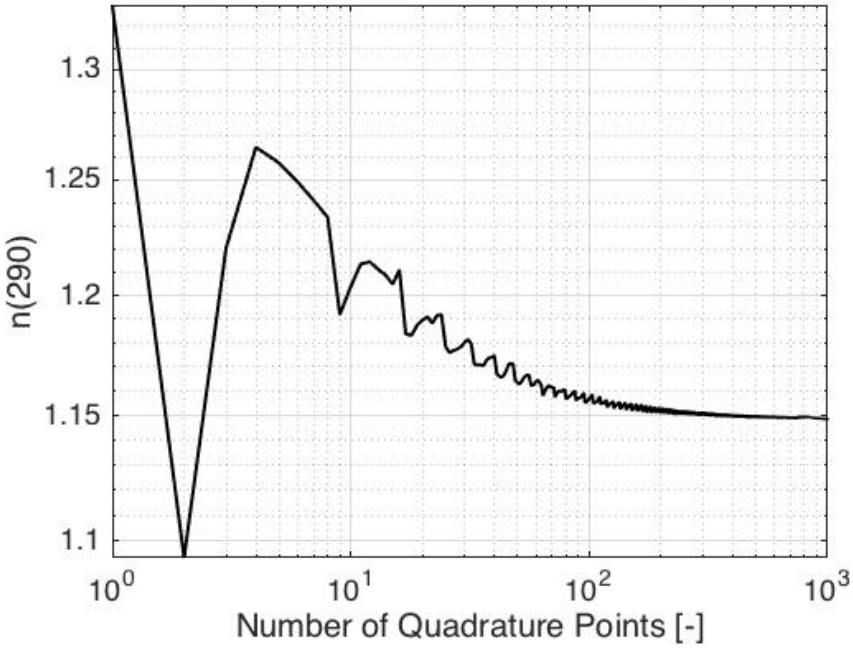

Fig. 10. Convergence of the trapezoidal quadrature of Eq. (9) for a refractive index at one specific wavenumber.

Efforts to improve the convergence by applying different quadrature algorithms have not been met with success. Specifically the QAWC adaptive integration algorithm for Cauchy principal values by Piessens et al. (1983) included in the GNU Scientific Library (GSL) by Galassi et al. (2009) did not achieve sufficient

accuracy and contained unphysical spikes in the real part of the spectra, despite the fact that it uses a 15-point Gauss-Kronrod integration rule and a 25-point modified Clenshaw-Curtis rule close to the singularity.

In order to validate the trapezoidal quadrature code based on Eq. (9) before its application to mineral dust, the real part of the refractive index spectrum of liquid water has been computed from its imaginary part and compared to literature data obtained by Segelstein (1981). The direct comparison of literature and computed values shows that both spectra are almost identical over the entire wavelength interval considered in this study and the application of the proposed computational procedure can thus be applied to other refractive index spectra with reasonable confidence.

A dust case comparison of the real part of the refractive index spectrum for a 0.5-µm particle from the northern Sahara is shown in Fig. 11. Generally both curves show qualitative agreement except for the longer wavelengths, where the Bruggeman EMA real part underestimates the refractive index and for very short wavelengths, where the difference is caused by the inclusion of the outlier data from Arakawa et al. (1997), which shows significant differences to the data of Glotch et al. (2007) and Egan and Hilgeman (1979) (see Fig. 2 for an illustrated comparison). Incidentally, the outmost short and long wave regions are also the bandwidths with the highest uncertainty in the dominant Silicate group spectrum, as can be seen in Fig. 2 and 3. The Figure 11 represents the final output spectrum of the present model for a 0.5-µm particle from the northern Sahara and can subsequently be used as an input for single-scattering calculations.

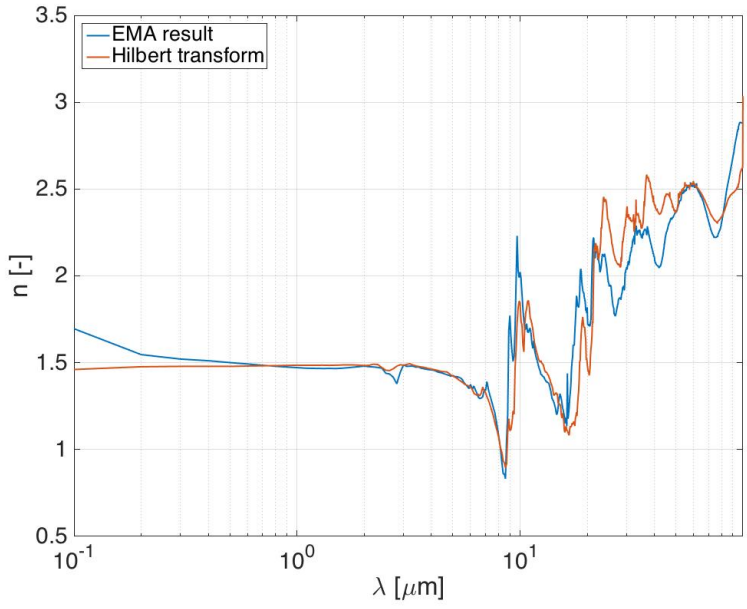

Fig. 11. Comparison of refractive index spectra (real part) obtained using the Bruggeman EMA (red) and the Hilbert transform of its corresponding imaginary part (blue) for a 1 micrometer particle from the northern Sahara region.

328 *5.2. Acceleration via the Fast Fourier Transform*

329 The slow convergence of the trapezoidal rule shown in Fig. 10 is undesirable in practice. Especially during
330 the computation of large optical property databases, a gain in efficiency in the computation of the refractive
331 index, however small, will accumulate to significant savings for the total computational cost. While the
332 introduction of a higher order quadrature scheme has failed, two other methods exist to improve the efficiency
333 of the numerical integration. First, the MapReduce algorithm by Dean and Ghemawat (2004) can be applied
334 to the trapezoidal quadrature and the calculations can thus be outsourced to a standard accelerator card where
335 they can be performed in parallel, leading to an increase in efficiency.
336 At a more fundamental level, the computations can also be made more efficient by reverting the derivation of
337 Toll (1956) and thus reformulate Eq. (9) in terms of a Fourier transform:

$$
\begin{aligned}
F\left\{\pi\left(n(\nu)-1\right)\right\} &= F\left\{P\int_{-\infty}^{\infty} k(\kappa)\cdot\frac{1}{\nu-\kappa}\,d\kappa\right\} \\
&= F\left\{k(\kappa)*\frac{1}{\kappa-\nu}\right\} \\
&= F\left\{k(\kappa)\right\}\cdot F\left\{\frac{1}{\nu-\kappa}\right\} \\
&= i\cdot\pi\cdot F\left\{k(\kappa)\right\}\cdot\mathrm{sgn}\left(\tilde{\nu}\right)
\end{aligned}
\tag{10}
$$

339 where *sgn* is the sign function and $\tilde{\nu}$ is the wavenumber ν in Fourier space. Equation (10) implicitly makes
340 use of the fact that the imaginary part of the refractive index is an even function of the wave number and of
341 the convolution theorem for Fourier transforms in the second step of the derivation. Through this
342 reformulation, the quadrature can be carried out efficiently by using the FFT algorithm of Cooley and Tukey
343 (1965), instead of the trapezoidal rule.

344 **6. First and Second Moments for AERONET size distributions**

345 With a procedure very similar to performing the Kramers-Kronig transform discussed in the preceding two
346 sections, it is feasible to compute the statistical moments of the regional refractive index spectra based on
347 local mineral dust aerosol size distributions retrieved from local AERONET measurements and thus compute
348 the expectation values of the refractive index spectra that are independent of the particle size. A summary of
349 the measurements is given by Dubovik et al. (2002), and representative size distributions have been selected
350 as a basis for the computation of the first and second moments of the refractive index spectra in the

geographical regions discussed in this study. Although Dubovik et al. (2002) extensively discusses measurement results in North Africa, the Middle East and America, necessary local size distributions are not available for all desired regions. In particular, no measurements from the continent of Asia are available. Consequently, suitable approximations need to be selected. For Northern and Southern Sahara, the data from Cap Verde are chosen, while for West Asia and East Asia the size distributions from Bahrain and Lanai (Hawaii) respectively are suggested. The reasoning for the Asian choice is given in Dubovik et al. (2002) and illustrated to a certain degree in Fig. 12, which shows a plot of the selected size distributions. It was articulated by Dubovik et al. (2002) that the measurements in Bahrain consist of a mixture of desert dust and pollution particles, while the measurements from Hawaii are influenced by long-range transported Asian dust.

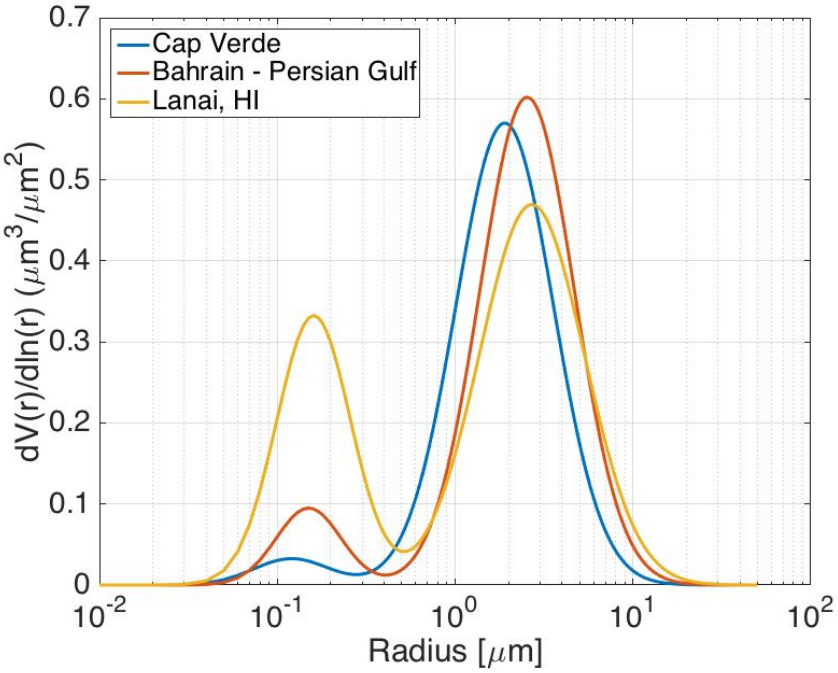

Fig. 12. Selection of bimodal size distributions from Dubovik et al. (2002) over the particle radius. On display are the distribution retrieved from AERONET measurements at Cap Verde, Bahrain, and Lanai.

Fig. 12 shows that all size distributions display a distinct bimodal structure, as is approximated by Eq. (11). This bimodality is least pronounced for the pure Saharan desert dust measured at Cap Verde. A larger proportion of smaller particles conjectured to originate from pollution manifests itself as a second smaller peak in the size distribution from Bahrain, although the distribution is still dominated by larger particles. The

368 measurement from Hawaii on the other hand shows a large number of smaller particles contributing to the
369 distribution. While this certainly includes a large number of sea spray aerosols, the smaller particles may also
370 be interpreted as soot or similar pollutants. In order to compute the moments, the bimodal size distribution fits
371 to the AERONET measurements need to be normalized to unity first, such that

372 $$C_N = \sum_{i=1}^{2} \int_0^{\infty} C_i \cdot \frac{1}{\sqrt{2\pi}\sigma_i} \cdot \exp\left(-\frac{\left(\ln(r) - \ln\left(r_i\right)\right)^2}{2 \cdot \sigma_i^2} \right) dr \qquad (11)$$

373 where C_N is the normalization constant, C_i are the scaling factors of the two Gaussian distributions, r_i are
374 the mean particle radii and σ_i are the standard deviations of the bimodal distribution, in correspondence with
375 the notation of Dubovik et al. (2002). The improper integral in Eq. (11) has an analytical solution that can be
376 found by substituting $u = \ln(r)$. The computed first and second moments are shown in Fig. 13a-d and
377 numerical results are provided as supplemental material to this study.

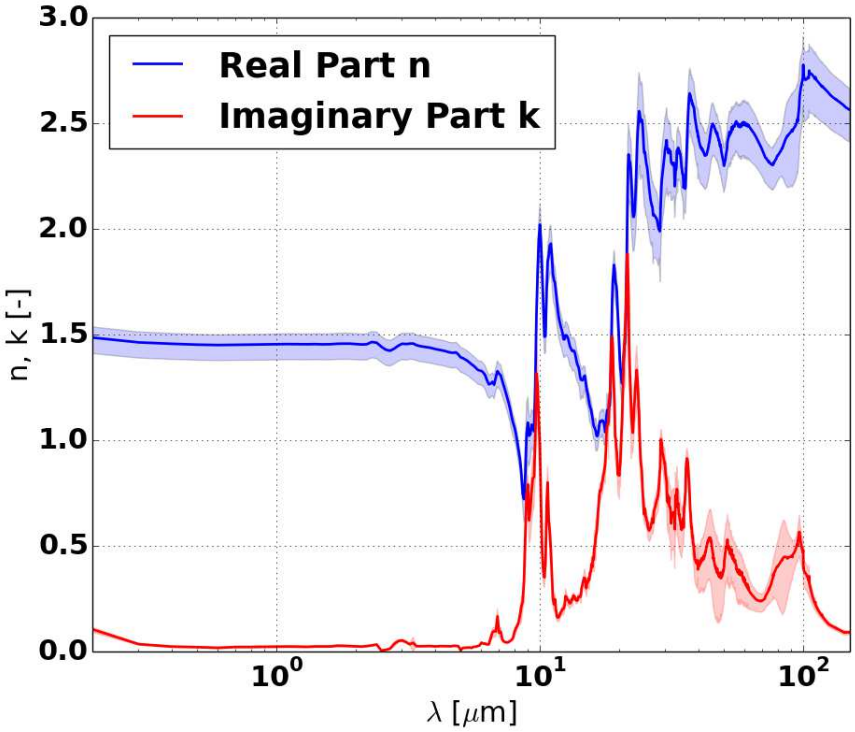

Fig. 13a. Mean and three standard deviations of North Saharan mineral dust refractive index spectra.

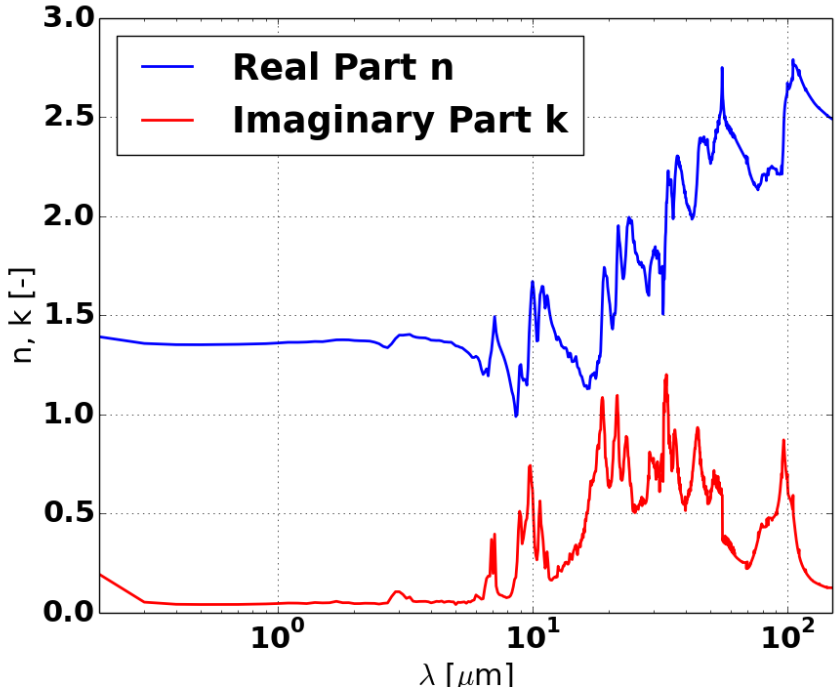

Fig. 13b. Mean complex refractive index spectrum for South Saharan mineral dust. The variance is zero.

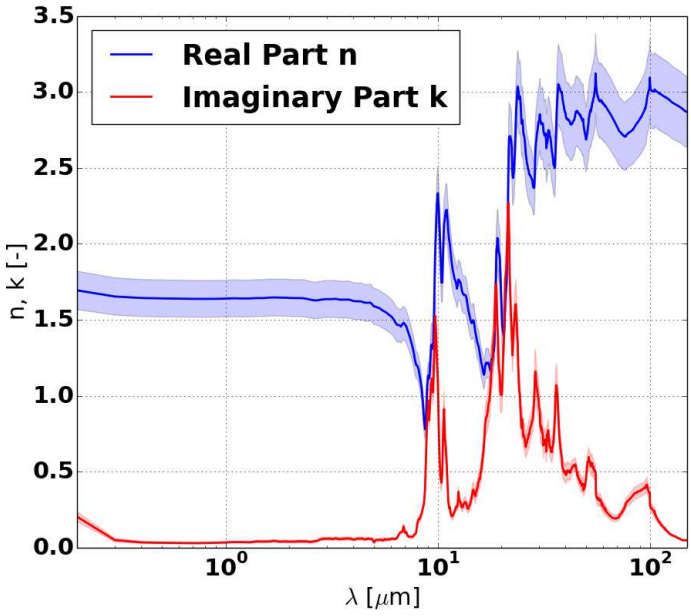

Fig. 13c. Mean and standard deviation of West Asian mineral dust refractive index spectra.

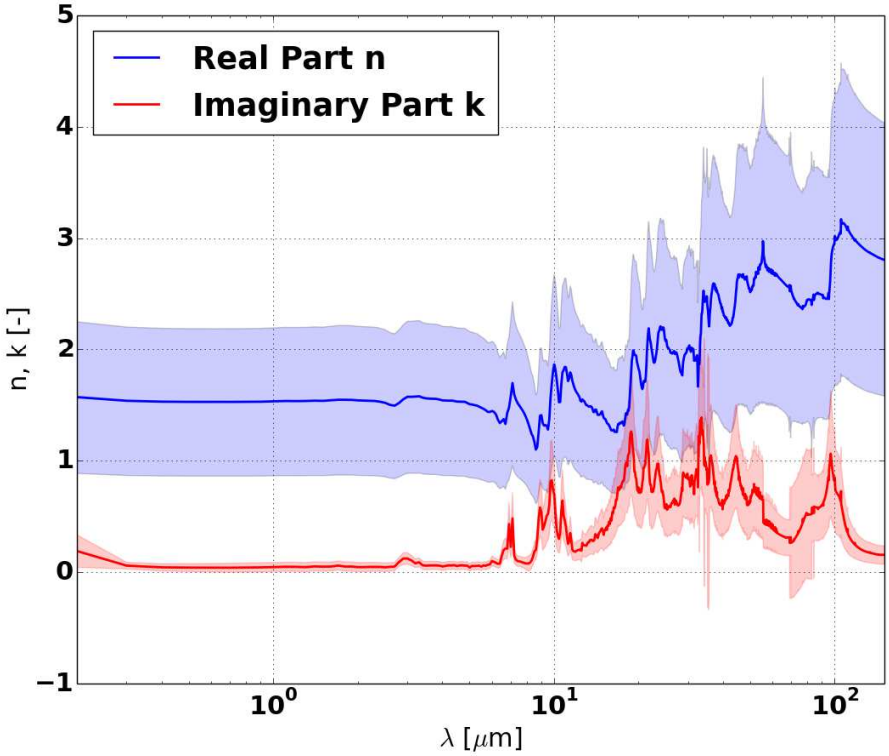

Fig. 13d. Mean and standard deviation of East Asian mineral dust refractive index spectra.

Fig. 13. Mean and standard deviation of the complex refractive index spectra of mineral dust in the regions North Sahara, South Sahara, West Asia, and East Asia based on particle size distributions inferred from AERONET measurements, as discussed by Dubovik et al. (2002). The mean is displayed as a full line, while the transparent area indicates a distance of three standard deviations from the mean.

Figs. 13a-d clearly show the expected increase of the standard deviation with a more expressed bimodality of the particle size distribution. The largest variance appears for the size distribution from Hawaii, as its two Gaussian peaks shown in Fig. 12 are of almost equal amplitude. In contrast, the variance for Saharan mineral dust shown in Figs. 13a-b is the smallest. As a consequence, the computed uncertainty in the refractive index for regions with strongly bimodal size distributions, such as the East Asian model of the present study shown in Fig. 13d suggests for the usage of size-resolved refractive indices for mineral dust particles. As there is no size-dependent composition data available for South Saharan mineral dust, its refractive index spectrum is identical for all sizes and its variance is artificially zero.

7. Conclusion

A new complex refractive index model was developed for Asian and Saharan mineral dust. This model improves upon existing work by calculating the refractive index as a function of the incident light wavelength, dust particle geometrical size or composition, and geographical region, as northern and southern Sahara, as well as western and eastern Asia are distinguished. The causality of the obtained refractive index spectra is ensured by applying a Hilbert transform to the imaginary part of the spectra. To this end, efficient algorithms have been developed to compute the EMA of a mineral mixture and to perform the subsequent Kramers-Kronig analysis.

Finally, the refractive index data collected for various chemical species and mineral types representative for mineral dust aerosols also enables the development of future models which may provide a more faithful representation of natural aerosol particles than the EMA, such as a Voronoi tessellation model proposed by Ishimoto et al. (2010) or a bicontinuous random medium described by Sahimi (2003).

Funding

This study was supported by the National Science Foundation (NSF) (AGS-1338440, AGS-1632209) and the National Oceanic and Atmospheric Administration (NOAA) (NA15NES4400003), and partially supported by the endowment funds associated with the David Bullock Harris Chair (02-51223110000) in Geosciences at the Texas A&M University.

Acknowledgments

The authors would like to thank Prof. Dr. Konrad Kandler from the TU Darmstadt and Dr. Martin Schnaiter from the KIT Karlsruhe for sharing their knowledge on aerosols and in particular Saharan mineral dust, as well as Dr. Steven Schroeder from the Texas A&M University for his careful review of the manuscript at hand.

References

Abadi, M., Agarwal, A., Barham, P., Brevdo, E., Chen, Z., Citro, C., Corrado, G. S., Davis, A., Dean, J., Devin, M., Ghemwat, S., Goodfellow, I., Harp, A., Irving, G., Isard, M., Jozefowicz, R., Jia, Y., Kaiser, L., Kudlur, M., Levenberg, J., Mané, D., Schuster,

M., Monga, R., Moore, S., Murray, D., Olah, C., Shlens, J., Steiner, B., Sutskever, I., Talwar, K., Tucker, P., Vanhoucke, V., Vasudevan, V., Viégas, F., Vinyals, O., Warden, P., Wattenberg, M., Wicke, M., Yu, Y., & Zheng, X. (2015). TensorFlow: Large-scale machine learning on heterogeneous systems, Software available from tensorflow.org, Retrieved: February 9, 2017.

Abel, N. H., (1881). Démonstration de l'impossibilité de la resolution algébraique des equations generals qui passent le quatrieme degré, in: Sylow, L., Lie, S., Oeuvres Completes de Niels Hendrik Abel I (2nd ed.), Grondahl & Son, pp. 66-87.

Ahnert, K., & Mulansky, M., (2011). odeint – Solving Ordinary Differential Equations in C++, ICNAAM 2011 AIP Conf. Proc., p. 1389

Arakawa, E. T., Tuminello, P. S., Khara, B. N., Millham, M. E., Authier, S., & Pierce, J., (1997). Measurement of optical properties of small particles, Scientific Conference on Obscuration and Aerosol Research Aberdeen Proving Ground, Maryland.

Badski, G., (2000). The OpenCV Library, Dr. Dobb's Journal of Software Tools, article id: 2236121.

Batten, C. E., (1984). Spectral optical constants of soots from polarized angular reflectance measurements, Appl. Opt. 24, pp. 1193-1199.

Bedidi, A., & Cervelle, B., (1993). Light scattering by spherical particles with hematite and goethitelike optical properties: effect of water impregnation, J. Geophys. Res. 98, pp. 11941-11952.

Bellman, R., & Wing, G. M., (1975). An introduction to Invariant Imbedding, New York: John Wiley & Sons.

Bi, L., Yang, P., Kattawar, G. W., & Mishchenko, M. I., (2013). Efficient implementation of the invariant imbedding T-matrix method and the separation of variables method applied to large nonspherical inhomogeneous particles, J. Quant. Spect. Rad. Trans. 116, pp. 169-183.

Blokh, A. G., (1988). Heat Transfer in Steam Boiler Furnaces, Hemisphere Publishing Corporation.

Bruggeman, D. A. G., (1935). Berechnung verschiedener physikalischer Konstanten von heterogenen Substanzen: 1. Dielektrizitätskonstanten und Wärmeleitfähigkeiten der Mischkörper aus isotropen Substanzen, Annalen der Physik, 5. Folge, Band 24, pp. 636-664. Transl.: Calculation of various physical constants of heterogeneous substances: 1. Dielectric permittivities and heat conductivities of mixed bodies made out of isotropic substances.

Carlson, T. N., & Benjamin, S. S., (1980). Radiative Heating Rates for Saharan Dust, J. Atmos. Sci. 37, pp. 193-213.

Chang, H., & Charalampopoulos, T. T., (1990). Determination of the Wavelength Dependence of Refractive Indices of Flame Soot, Proc. Roy. Soc. Math. Phys. Sci. 430(1880), pp. 577-591.

Chin, M., Ginoux, P., Lucchesi, R., Huebert, B., Weber, R., Anderson, T., Masonis, S., Blomquist, B., Bandy, A., & Thornton D., (2003). A global aerosol model forecast for the ACE-Asia field experiment, J. Geophys. Res. 108(D23), 8654, doi:10.1029/2003JD003642.

Cooley, J. W., & Tukey, J. W., (1965), An algorithm for the machine calculation of complex Fourier series, Math. Comp. 19, pp. 297-301. doi:10.1090/S0025-5718-1965-0178586

Dean, J., & Ghemawat, S., (2004). MapReduce: Simplified Data Processing on Large Clusters, OSDI'04: Sixth Symposium on Operating System Design and Implementation, San Francisco, CA.

Di Bagio, C., Boucher, H., Caquineau, S., Chevaillier, S., Cuesta, J., & Formenti, P., (2014), Variability of the infrared complex refractive index of African mineral dust: Experimental estimation and implications for radiative transfer and satellite remote sensing, Atmos. Chem. Phys. 14, pp. 11093-11116.

Dubovik, O., Hoben, B., Eck, T. F., Smirnov, A., Kaufman, Y. J., King, M. D., Tanré, D., & Slutsker, I., (2002). Variability of Absorption and Optical Properties of Key Aerosol Types Observed in Worldwide Locations, J. Atmos. Sci. 59, pp. 590-608.

Dubovik, O., Sinyuk, A., Lapyonok, T., Holben, B. H., Mishchenko, M., Yang, P., Eck, T. F., Volten, H., Munoz, O., Veihelmann, B., van der Zande, W. J., Leon, J.-F., Sorokin, M., & Slutsker, I., (2006). Application of spheroid models to account for aerosol particle nonsphericity in remote sensing of desert dust. J. Geophys. Res. 111, D11208, doi:10.1029/2005JD006619.

Egan, W. G., & Hilgeman, T. W., (1979). Optical Properties of Inhomogeneous Materials, New York: Academic Press, pp. 235.

Formenti, P., Schütz, L., Balkanski, Y., Desboeufs, K., Ebert, M., Kandler, K., Petzold, A., Scheuvens, D., Weinbruch, S., & Zhang, D., (2011). Recent progress in understanding physical and chemical properties of African and Asian mineral dust, Atmos. Chem. Phys. 11, pp. 8231-8256.

Geng, H., Park, Y., Hwang, H., Kang, S., & Ro, C.-U., (2009). Elevated nitrogen-containing particles observed in Asian dust aerosol samples collected at the marine boundary layer of the Bohai Sea and Yellow Sea, Atmos. Chem. Phys. 9, pp. 6933-6947.

Gillespie, J. B., & Lindberg, J. D., (1992): Ultraviolet and visible imaginary refractive index of strongly absorbing atmospheric particulate matter, Appl. Opt. 31, pp. 2112-2115.

Glotch, T. D., Rossman, G. R., & Aharonson, O., (2007). Mid-infrared (5-200 μm) reflectance spectra and optical constants of ten phyllosilicate minerals, Icarus 192, pp. 605-622.

Harrington, P., (2012). Machine Learning in Action, Shelter Island: Manning Publications.

Hasti, T., Tibshirani, R., & Friedman, J., (2009). The Elements of Statistical Learning, New York: Springer Science+Business Media.

Henning, T., Begemann, B., Mutschke, H., & Dorschner, J., (1995): Optical properties of oxide dust grains, Astron. and Astrophys. Suppl. Ser. 112, pp. 143.

Hess, M., Koepke, P., & Schult, I., (1998). Optical Properties of Aerosols and Clouds: The Software Package OPAC, Bull. Am. Met. Soc. 79, pp. 831-844.

Ishimoto, H., Zaizen, Y., Uchiyama, A., Masuda, K., & Mano, Y., (2010). Shape modeling of mineral dust particles for light-scattering calculations using the spatial Poisson-Voronoi tessellation, J. Quant. Spect. Rad. Trans. 111, pp. 2434-2443.

Ivlev, L. S., & Popova, S. I., (1972). The complex refractive indices of substances in the atmospheric aerosol dispersed phase, Izv. Atmos. Oceanic Phys. 9, pp. 587-591.

Iwabuchi, H., & Yang, P., (2011). Temperature dependence of ice optical constants: Implications for simulating the single-scattering properties of cold ice clouds, J. Quant. Spec. Rad. Trans. 112, pp. 2520-2525.

Jarzembski, M. A., Norman, M. L., Fuller, F. A., Srivastava, V., & Cutten, D. R., (2003). Complex refractive index of ammonium nitrate in the 2-20μm spectral range, Appl. Opt. 42(6), pp. 922-930.

Jurewicz, A., Orofino, V., Marra, A. C., & Blanco, A., (2003). Optical constants of powdered limestone obtained by taking into account the grain shapes: Applicability to Martian studies, Astron. & Phys. 410, pp. 1055-1062.

Kahnert, M., (2004). Reproducing the optical properties of fine desert dust aerosols using ensembles of simple model particles, J. Quant. Spect. Rad. Trans. 85, pp. 231-249.

Kandler, K., Schütz, L., Deutscher, C., Ebert, M., Hofmann, H., Jäckel, S., Jaenicke, R., Knippertz, P., Lieke, K., Massling, A., Petzold, A., Schladitz, A., Weinzierl, B., Wiedensohler, A., Zorn, S., & Weinbruch, S., (2009). Size distribution, mass concentration, chemical and mineralogical composition and derived optical parameters of the boundary layer aerosol at Tinfou, Morocco, during SAMUM 2006, Tellus 61B, pp. 32-50.

Klaver, A., Formenti, P., Caquineau, S., Chevaillier, S., Ausset, P., Calzolai, G., Osborne, S., Johnson, B., Harrison, M., & Dubovik, O., (2011), Physico-chemical and optical properties of Sahelian and Saharan mineral dust: in situ measurements during the GERBILS campaign, Quart. J. Royal Met. Soc. doi:10.1002/qj.889

Koven, C. D., & Fung, I., (2008). Identifying global dust source areas using high-resolution land surface form, J. Geophys. Res. 113, pp. D22204:1-19

Levoni, C., Cervoni, M., Guzzi, R., & Torricella, F., (1997). Atmospheric aerosol optical properties: a database of radiative characteristics for different components, Applied Optics 36, pp. 8031-8041.

Lindelöf, E., (1894). Sur l'application de la method des approximations successives aux equations différentielles ordinaires du premier ordre, Comptes rendus hebdomadaires des séances de l'Académie des sciences 116, pp. 454-457.

Liu, C., Panetta, L., Yang, P., Macke, A., & Baran, A. J., (2013). Modeling the scattering properties of mineral aerosols using concave fractal polyhedra, Applied Optics 52, pp. 640-652.

Long, L. L., Querry, M. R., Bell, R. J., & Alexander, R. W., (1993). Optical properties of calcite and gypsum in crystalline and powdered form in the infrared and far-infrared, Infrared Phys. Tech. 34, pp. 191-201.

Longtin, D. R., Shettle, E. P., Hummel, J. R., & Pryce, J. D., (1988). A Wind Dependent Desert Aerosol Model: Radiative Properties, Scientific Report No. 6, Air Force Geophysics Laboratory, Hanscom Airforce Base, Massachusetts.

Ma, Q., Liu Y., Liu, C., Ma, J., & He, H., (2012). A case study of Asian dust storm particles: Chemical composition, reactivity to SO_2 and hygroscopic properties, J. Env. Sci. 24, pp. 62-71.

Malitson, I. H., (1965). Interspecimen Comparison of the Refractive Index of Fused Silica, J. Opt. Soc. Am. 55(10), pp. 1205-1209.

Marra, A. C., Blanco, A., Fonti, S., Jurewicz, A., & Orofino, V., (2005). Fine hematite particles of Martian interest: absorption spectra and optical constants, J. Phys.: Conf. Ser. 6, doi:10.1088/1742-6596/6/1/013

Maxwell Garnett, J. C., (1904). Colours in Metal Glasses and in Metallic Films, Phil. Trans. Royal Soc. A 203, pp. 359-371. doi:10.1098/rsta.1904.0024

Mishchenko, M. I., Travis, L. D., Kahn, R. A., & West, R. A., (1997). Modeling phase functions for dustlike tropospheric aerosols using a shape mixture of randomly oriented polydisperse spheroids, J. Geophys. Res.-Atmos. 102, pp. 16831-16847.

Mooney, T., & Knacke, R. F., (1995). Optical constants of chlorite and serpentine between 2.5 and 50 microns, Icarus 64, p. 493-502.

Mori, I., Nishikawa, M., Tanimura, T., & Quan, H., (2003). Change in size distribution and chemical composition of kosa (Asian dust) aerosol during long-range transport, Atmos. Env. 37, pp. 4253-4263.

Myhre, G., & Stordal, F., (2001). Global sensitivity experiments of the radiative forcing due to mineral aerosols, J. Geophys. Res.-Atmos. 106, pp. 18193-18204, doi:10.1029/2000jd900536.

Natsuyama, H. H., Ueno, S., & Wang, A. P., (1998). Terrestrial Radiative Transfer, Tokyo: Springer-Verlag.

Onari, S., Arai, T., & Kudo, K., (1977). Infrared Lattice vibrations and dielectric dispersion in α–Fe_2O_3, Phys. Rev. B 16, pp. 1717-1721.

Otto, S., Bierwirth, E., Weinzierl, B., Kandler, K., Esselborn, M., Tesche, M., Schladitz, A., Wendisch, M., & Trautmann, T., (2009). Solar radiative effects of a Saharan dust plume observed during SAMUM assuming spheroidal model particles, Tellus 61B, pp. 270-296, doi: 10.1111/j.1600-0889.2008.00389

Palmer, K. F., & Williams, D., (1975). Optical constants of sulfuric acid: application to the clouds of Venus, Appl. Opt. 14, pp. 208-219.

Patterson, E. M., Gillete, P. A., & Stockton, H. H., (1977). Complex index of refraction between 300 and 700 nm for Saharan aerosols, J. Geophys. Res. 82, pp. 3153-3160.

Peterson, J. T., & Weinman, J. A., (1969). Optical properties of quartz dust particles in infrared wavelength, J. Geophys. Res. 28, 6947-6952.

Petzold, A., Rasp, K., Weinzierl, B., Esselborn, M., Hamburger, T., Dörnbrack, A., Kandler, K., Schütz, L., Knippertz, P., & Fiebig, M., (2009). Saharan dust absorption and refractive index from aircraft-based observations during SAMUM 2006, Tellus 61B, pp. 118-130.

Philipp, H. R., (1985). Handbook of Optical Constants of Solids, San Diego: Academic Press, Inc., pp. 719-747.

Piessens, R., de Doncker-Kapenga, E., Überhuber, C. W., & Kahaner, D., (1983). QUADPACK: A subroutine package for automatic integration, Springer-Verlag Berlin-Heidelberg

Polo, J., & Estalayo, G., (2015). Impact of atmospheric aerosol loads on Concentrating Solar Power production in arid-desert sites, Solar Energy 115, pp. 621-631.

Popova, S. I., Tolstkh, T. S., & Vorobev, V. T., (1972). Optical characteristics of amorphous quartz in the 1400-200/cm region, Opt. Spectrosc. 33, pp. 143-144.

539 Prospero, J. M., Ginoux, P., Torres, O., Nicholson, S. E., & Gill, T. E., (2002). Environmental characterization of global sources of
540 atmospheric soil dust identified with the Nimbus 7 Total Ozone Mapping Spectrometer (TOMS) absorbing aerosol product, Rev. of
541 Geophys. 40, pp. 1002.
542 Querry, M. R., Osboren, G., Lies, K., Jordon, R., & Coveney, R. M., (1978). Complex refractive index of limestone in the visible and
543 infrared. Appl. Opt. 17, pp. 353-356.
544 Querry, M. R., (1985). Optical constants, US Army CRDEC, Contractor Report, Aberdeen Proving Ground, MD .
545 Querry, M. R., (1987). Optical constants of minerals and other materials from the millimeter to the UV, Rep. CRDEC-CR-88009, US
546 Army, Aberdeen Proving Ground, MD.
547 Roush, T., Pollack, J., & Orenberg, J., (1991). Derivation of mid-infrared optical constants of some silicate and palagonite, Icarus 94, pp.
548 191-208.
549 Ryder, C. L., Highwood, E. J., Rosenberg, P. D., Trembath, J., Brooke, J. K., Bart, M., Dean, A., Crosier, J., Dorsey, J., Brindley, H.,
550 Banks, J., Marsham, J. H., MacQuaid, J. B., Sodemann, H., & Washington, R., (2013), Optical properties of Saharan dust aerosol
551 and contribution from coarse mode as measured during the Fennec 2011 aircraft campaign, Atmos. Chem. Phys. 13, pp. 303-325.
552 Sahimi, M., (2003). Heterogeneous Materials I, Linear Transport and Optical Properties, New York: Springer Verlag.
553 Schroedter-Homscheidt, M., Oumbe, A., Benedetti, A., & Morcrette, J.-J., (2013). Aerosols for concentrating solar electricity production
554 forecasts, Bull. Am. Met. Soc. pp. 903-914.
555 Segelstein, D., (1981). The Complex Refractive Index of Water, M.Sc. Thesis, University of Missouri, Kansas City. Data available for
556 download at: www.philiplaven.com/Segelstein.txt
557 Shell, K. M., & Somerville, R. C. J., (2007). Direct radiative effect of mineral dust and volcanic aerosols in a simple aerosol climate
558 model, J. Geophys. Res. 112, pp. D03205:1-15
559 Shettle, E. P., & Fenn, R. W., (1979). Models of the aerosols of the lower atmosphere and the effects of humidity variations on their
560 optical properties, Project 7670, US Air Force Geophys. Lab., MD.
561 Smith, R., (2007). An Overview of the Tesseract OCR Engine, ICDAR '07 Proceedings of the Ninth International Conference on
562 Document Analysis and Recognition – Volume 02, pp. 629-633.
563 Sokolik, I. N., Winker, D. M., Bergametti, G., Gillete, D. A., Carmichael, G., Kaufman, Y. J., Gomes, L., Schuetz, L., & Penner, J. E.,
564 (2001). Introduction to special section: Outstanding problems in quantifying the radiative impacts of mineral dust, J. Geophys. Res.-
565 Atmos. 106, pp. 18015-18027, doi:10.1029/2000jd900498.
566 Stagg, B. J., & Charalampopoulos, T. T., (1993). Refractive Indices of Pyrolytic Graphite, Amorphous Carbon, and Flame Soot in the
567 Temperature Range 25o-600o C, Comb. and Flam. 94, pp. 381-396.
568 Steyer, T. R., Day, K. L., & Huffman, D. R., (1974): Infrared absorption by small amorphous quartz sphere, Appl. Opt. 13, pp. 1586-
569 1590.
570 Toll, J. S., (1956). Causality and the Dispersion Relation: Logical Foundations, Phys. Rev. 104, pp. 1760-1770. doi:
571 https://doi.org/10.1103/PhysRev.104.1760
572 Toon, O. B., Pollack, J. B., & Sagan, C., (1977). Physical properties of the particles composing the Martian dust storm of 1971-1972,
573 Icarus 30, pp. 663-696.
574 Tropf, W., (1998). Handbook of Optical Constants of Solids, Sand Diego, CA: Elsevier Academic, pp. 653-682.
575 Volz, F. E., (1973). Infrared optical constants of ammonium sulfate, Sahara dust, volcanic pumice, and fly ash, Appl. Opt. 12, pp. 564-
576 568.
577 Warren, S. G., (1984). Optical constants of ice from the ultraviolet to the microwave, Appl. Opt. 23, pp. 1206-1225.
578 Wagner, R., Ajtai, T., Kandler, K., Lieke, K., Linke, C., Müller, T., Schnaiter, M., & Vragel, M., (2012). Complex refractive indices of
579 Saharan dust samples at visible and near UV wavelengths, Atmos. Chem. Phys. 12, pp. 2491-2512. doi:10.5194/acp-12-2491-2012

Yue, X., Wang, H. Wang. Z., & Fan, K., (2009). Simulation of dust aerosol radiative feedback using the Global Transport Model of Dust: 1. Dust cycle and validation, J. Geophys. Res. 114, pp. D10202:1-24

Zukic, M., Douglas, G. T., Spann, J. F., & Torr, M. R., (1990). Vacuum ultraviolet thin films. 1: Optical constants of BaF2, CaF2, LaF3, MgF2, Al2O3, HfO2, and SiO2 thin films, Appl. Opt. 29(28), 4284-4292.

Appendix A. Code

Both the code for the EMA calculation, as well as the Hilbert transform are open-source under the GNU General Public License Version 3 GPLv3: https://www.gnu.org/copyleft/gpl.html

The C++ source code can be cloned from the following online repository:

repository link: https://github.com/PStegmann/Bruggeman_Effective_Medium

Appendix B. Regional size-dependent mineral dust grain composition

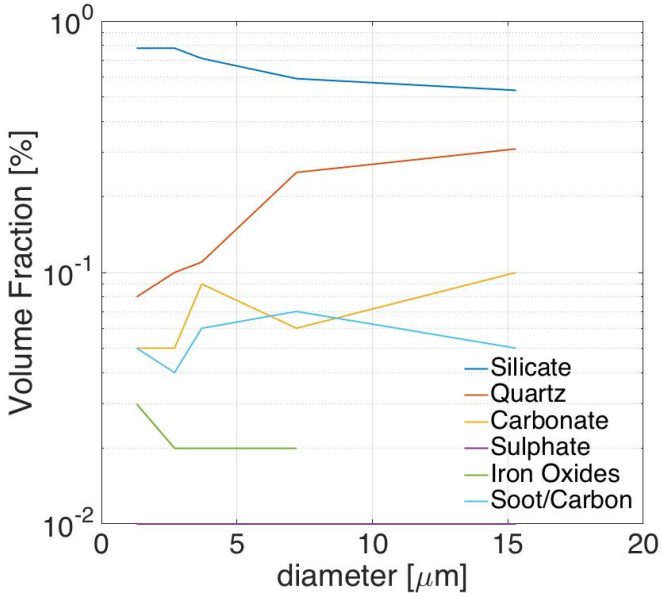

Fig. B1. Size dependence of the mineral composition for western Asia.

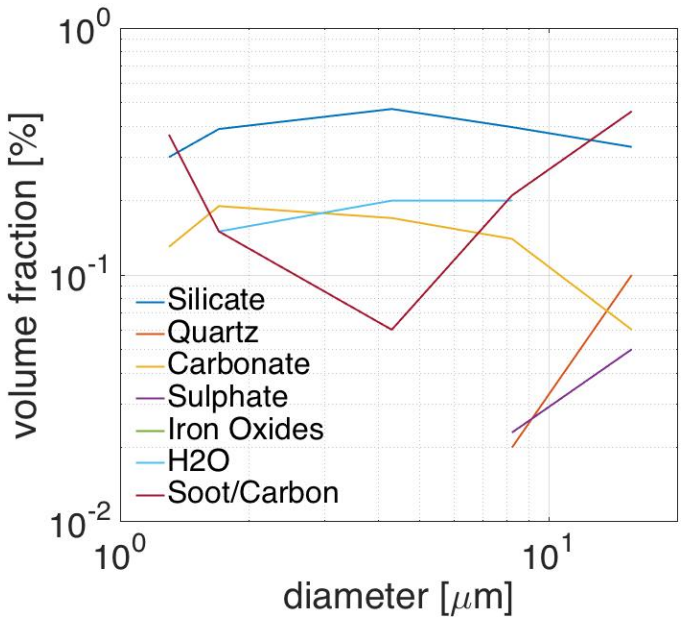

Fig. B2. Size dependence of the mineral composition for eastern Asia.

Table B1. Mineral composition of south Saharan mineral dust. No size-dependent data available.

Mineral group	Volume fraction [%]
Silicates	89
Quartz	6
Sulphates	1
Iron oxides	4

Appendix C. Real part of the refractive index spectra for mineral groups

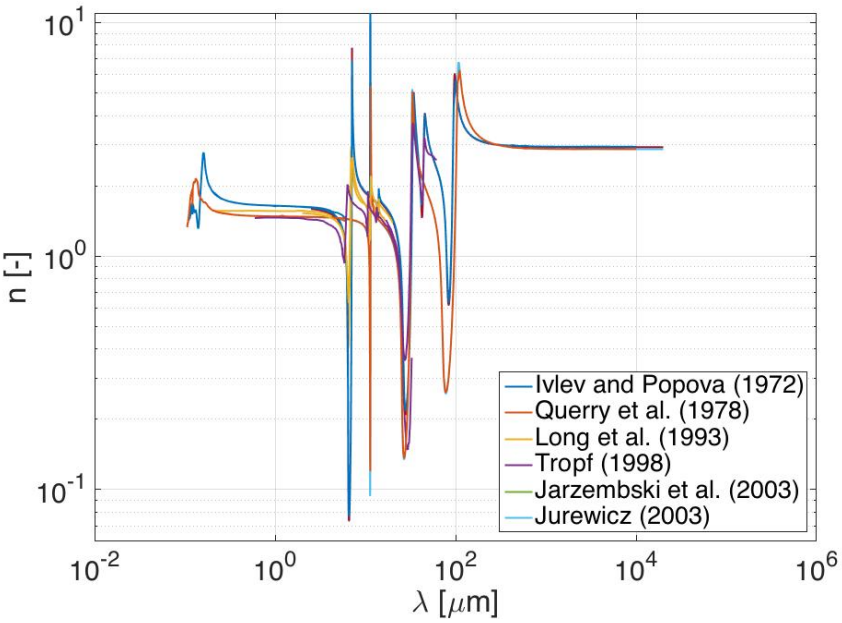

597

598 Fig. C1. Real part of the refractive index spectrum of the Carbonate group.

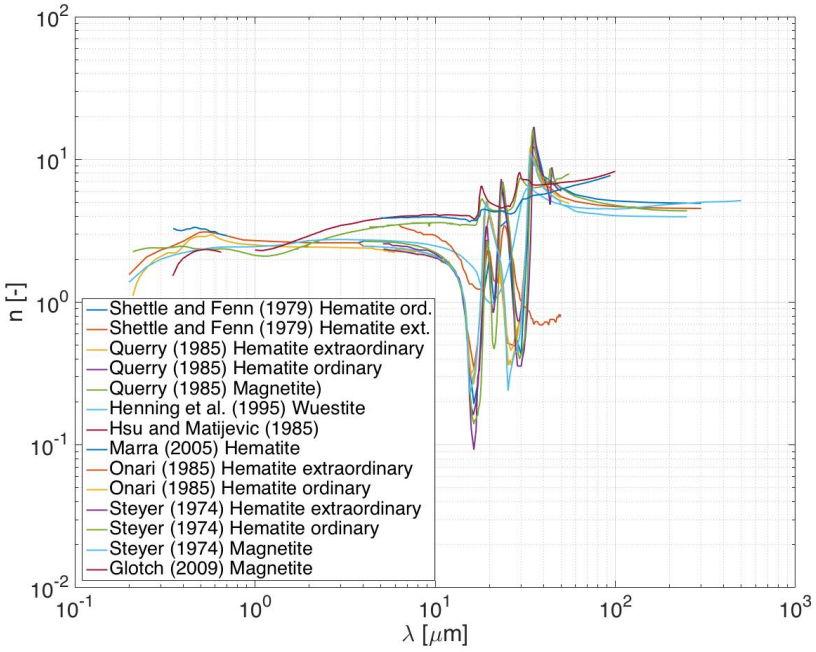

599

Fig. C2. Real part of the refractive index spectrum of the iron oxides group.

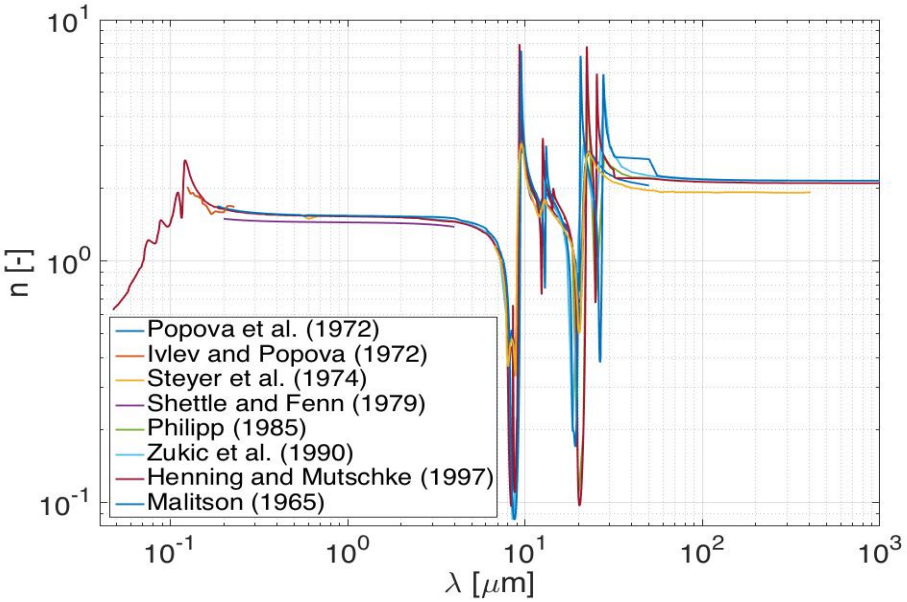

Fig. C3. Real part of the refractive index spectrum of the Quartz group.

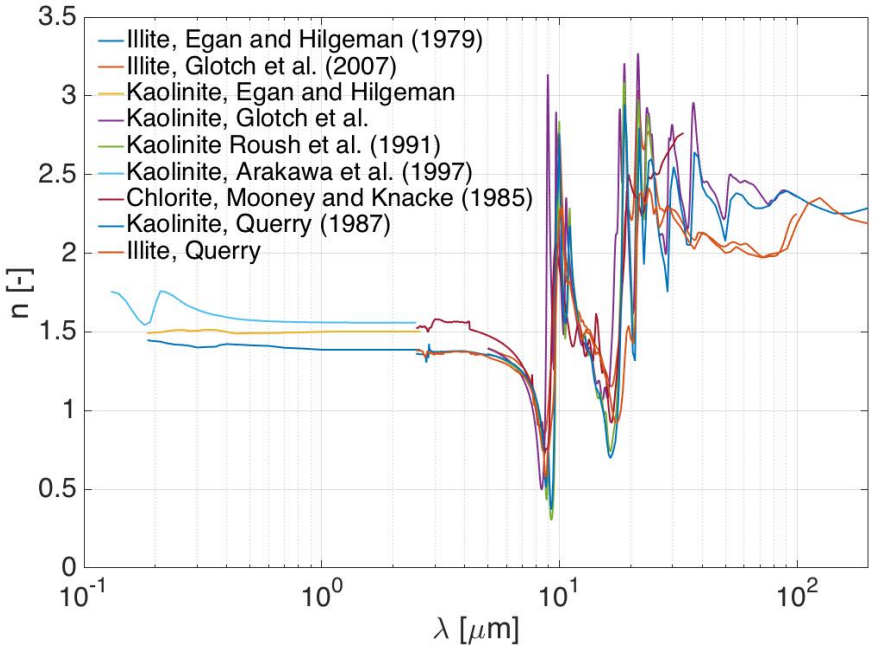

604 Fig. C4. Real part of the refractive index spectrum of the Silicate group

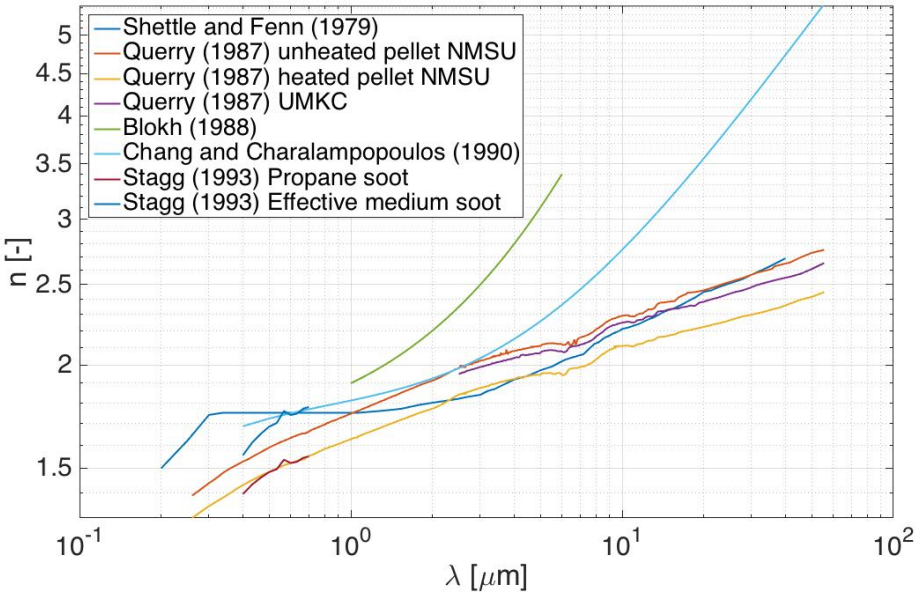

605

606 Fig. C5. Real part of the refractive index spectrum of the soot group.

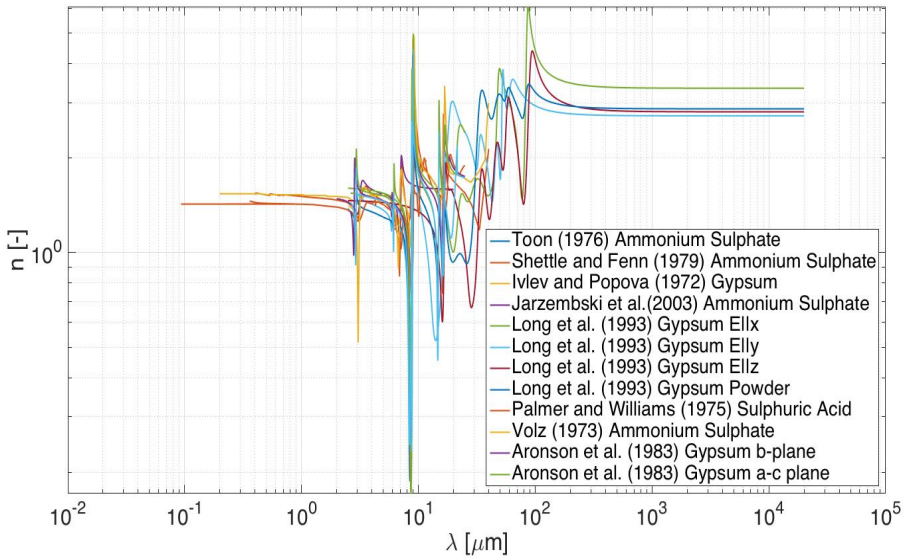

607

608 Fig. C6. Real part of the refractive index of the Sulphate group.